Frontiers in Earth Science

TYPE Original Research
PUBLISHED 12 February 2025
DOI 10.3389/feart.2025.1538324

EDITED BY
Eleftheria Papadimitriou,
Aristotle University of Thessaloniki, Greece

REVIEWED BY
Zhaofeng Wang,
Chinese Academy of Sciences (CAS), China
Cun Zhang,
China University of Mining and Technology, Beijing, China

*CORRESPONDENCE
Xuefeng Gao,
✉ tbh398@cumt.edu.cn
Dan Ma,
✉ dan.ma@cumt.edu.cn

RECEIVED 02 December 2024
ACCEPTED 17 January 2025
PUBLISHED 12 February 2025

CITATION
Li Z, Zhang Y, Gao X, Ma D, Fan L, Li G, Li X, He M and Cheng Z (2025) Characterizing the deformation, failure, and water-conducting fractures evolution of shallow weakly cemented overburden under coal mining. *Front. Earth Sci.* 13:1538324. doi: 10.3389/feart.2025.1538324

Characterizing the deformation, failure, and water-conducting fractures evolution of shallow weakly cemented overburden under coal mining

Zhenhua Li[1], Yandong Zhang[2], Xuefeng Gao[1,3]*, Dan Ma[1,3]*, Limin Fan[3], Guodong Li[4], Xiaolei Li[5], Min He[6] and Zheng Cheng[7]

[1]School of Energy Science and Engineering, Henan Mine Water Disaster Prevention and Control and Water Resources Utilization Engineering Technology Research Center, Henan Polytechnic University, Jiaozuo, Henan, China, [2]Shenhua New Street Energy Co., Ltd, Ordos, China, [3]School of Mines, MOE Key Laboratory of Deep Coal Resource Mining, China University of Mining and Technology, Xuzhou, China, [4]Jiaozuo Coal Group Co., Ltd., Jiaozuo, China, [5]Jiaozuo Coal Industry (Group) Xinxiang Energy Co., Ltd., Jiaozuo, China, [6]Xinqiao Coal Mine of Yongmei Group Co., Ltd, Shangqiu, China, [7]Zhengzhou Coal Industry (Group) Yanghe Coal Industry Co., Ltd., Xinmi, China

Understanding the collapse mechanisms of shallow, multi-layered, weakly cemented overburden is key to safe and efficient coal mining in central and western China. Hence, we conducted a meter-scale similar physical model experiment using high-resolution digital speckle technology to replicate the deformation and failure patterns of shallowly buried, weakly cemented overburden under mining activities, and to determine the initiation, development, and stability of water-conducting fractures. Additionally, a site-scale numerical model was developed to allow for the examination of the stress-displacement evolution within the weakly cemented overburden. The results indicate that the maximum vertical displacements at key locations such as the basic roof, the weakly cemented critical layer, and the surface were 8.9 m, 8.65 m, and 8.2 m, respectively. The collapse step distance of the basic roof was 22.4 m, and the maximum collapse height reached 48 m. After the weakly cemented critical layer failed, the overlying strata collapsed accordingly, with the actual water-conducting fracture zone reaching a maximum height of 96.3 m. After the completion of coal mining, the overburden experienced four periodic collapses. As the working face advanced, the overburden in the center of the mined-out area showed a state of stress release, while the overburden on both sides exhibited stress concentration. The maximum vertical stresses in the siltstone and sandstone were 6.7 MPa and 1.9 MPa, with stress concentration factors of 2.2 and 0.6, respectively. This study provides valuable insights into the safety management of weakly cemented overburden.

KEYWORDS

weakly cemented overburden, overburden failure, water-conducting fractures, similar physical model, coal mining

1 Introduction

The focus of coal production in China is gradually shifting to the central and western regions, where coal output accounting for more than 70% of the country's total production (Zhang C. et al., 2023; Liu et al., 2024). However, most coal mines in the central and western regions of China are characterized by thin bedrock, shallow burial, and thick coal seams, with the mines themselves exhibiting large-scale and high extraction intensity. As a result, the movements, deformation, and failure of shallow overburden caused by mining activities are more intense than those in coal mining faces in other regions (Di, 2022; Zhu L. et al., 2022). At the same time, the ecological environment in the western mining areas of China is fragile (Li et al., 2023), and high-intensity underground mining activities will lead to a decline in the underground ecological water table, causing environmental degradation and other issues (Wu et al., 2024).

In recent years, several mines primarily targeting Jurassic and Cretaceous coal seams have been built in the central and western regions of China (Zhang L. et al., 2023). Due to a relatively short diagenetic period, these strata exhibit a higher porosity between particles, poor cementation, and lower strength compared to similar rocks in the eastern regions, and are prone to disintegration and mud formation when in contact with water (Zhang G. et al., 2022; Zhang S. et al., 2022). Therefore, shallowly buried, exceptionally thick coal seams in the western regions are prone to inducing surface cracking, ground subsidence, and spontaneous coal combustion during the mining process (Liu et al., 2022; Zhang J. et al., 2022; Dong et al., 2024). The water-conducting fractures formed in the roof after mining can connect with overlying aquifers, greatly increasing the risk of water inrush disasters (Ma et al., 2022; Liu et al., 2023; Ma et al., 2023). Therefore, a key challenge is to clarify the deformation and failure characteristics of shallow, poorly cemented overburden under mining-induced stress and to understand the evolution of water-conducting fractures. This understanding is essential for ensuring the safe extraction of coal from the central and western coal mines of China.

Weakly cemented rock layers are mainly found in the Jurassic and Cretaceous strata in the western mining areas of China (Zhang L. et al., 2023). The mechanical properties, structural characteristics, and movement patterns of weakly cemented rock layers have received considerable attention. For example, Yan et al. (2020) found that rocks with poor cementation exhibit localized failure under pressure, and the resulting sand particles display better uniformity. Meng et al. (2021) studied the mechanical properties of clay-rich, weakly cemented soft rocks under dynamic impact and found that a moisture content of 10% marks the critical threshold between brittle and plastic failure. Furthermore, Wang et al. (2018) conducted uniaxial and acoustic emission tests on weakly cemented sandstone with different bedding angles collected from the Xiaojihan coal mine, finding that larger bedding angles resulted in fewer large-scale fractures. Zheng et al. (2015) conducted creep tests on porous sandstone and observed that the rock samples exhibited varying creep behaviors under different stress components. Taking into account the viscous volumetric deformation, they developed a corresponding creep model. Some researchers have begun to focus on the movement behavior of weakly cemented rock layers. Yang and Xia (2018) examined the failure mechanisms and mining pressure characteristics of weakly cemented overburden, proposing appropriate control measures. Zhang et al. (2020) investigated the movement laws of ultra-thick weakly cemented overburden and found that the failure mode of weakly cemented thin overburden is beam-like, while thick weakly cemented overburden exhibits a shell-like failure.

The formation of water-conducting fractures is a key phenomenon in the deformation and failure of weakly cemented overburden significantly impacting the ecological safety of groundwater in mining areas (Li A. et al., 2022; Zheng et al., 2024). Therefore, researchers have conducted numerous studies on the distribution characteristics of water-conducting fracture zones and the factors influencing their development height. For instance, Xu et al. (2021) proposed an intelligent statistical model to assess the rock mass damage rate under varying moisture contents based on laboratory experiments, and introduced a predictive model for the height of these zones based on the elastic modulus. Li et al. (2018) used the UDEC code to study the distribution of fracture and stress fields in the overburden under three different mining methods: without coal pillars, top-coal caving, and protective layer mining. The fracture shapes were found to be trapezoidal, triangular, and tower-shaped, respectively. Wang X. et al. (2021) developed an equation to calculate the maximum span of an unsupported roof under both faulted and non-faulted conditions and compared the results with numerical simulations. They found that the height of the water-conducting fracture zone increased significantly in the presence of faults, approximately 1.5 times greater than that in the non-faulted condition. Zha et al. (2020) designed a hydro-mechanical coupling experimental system to simulate the evolution of damaged fractures and the migration of groundwater in weakly cemented rock layers during mining. Their results showed that the infiltration rate of surface water increased steadily during the mining process. Despite the efforts of experiments, simulations, and geological surveys to improve understanding of the deformation and failure mechanisms of weakly cemented overburden, the collapse characteristics of shallow-buried, multi-layer weakly cemented overburden and the evolution of water-conducting fractures remain an open question.

To address this question, we conducted a physical model experiment at a meter scale, based on real geological conditions, using digital speckle technology to capture the movement, deformation, and failure of shallowly buried, multilayered weakly cemented rock formations. We analyzed the formation, evolution, and stabilization of water-conducting fractures in these layers under mining activities. Additionally, we employed a site-scale mining mechanical model to examine the stress and displacement evolution within the weakly cemented layers and quantify the development of fracture zones. These findings contribute to closing the knowledge gap regarding the deformation of surrounding rock and the formation of water-inrush hazards in weakly cemented overburden coal mines in western China.

2 Materials and methods

2.1 Geologic background

Yushuling Coal Mine is a typical example of a shallowly buried, weakly cemented overburden mining area in China, making the study of its fracture zone development highly relevant.

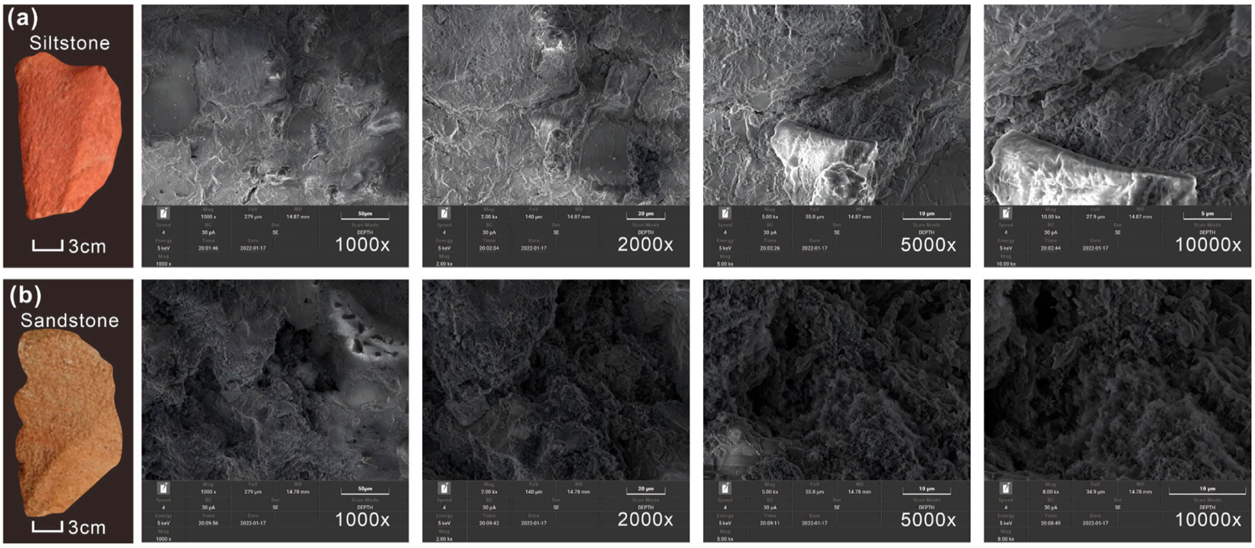

FIGURE 1
Micro-pore structure characteristics of **(A)** siltstone and **(B)** sandstone under different magnification.

The primary strata in the mine include Triassic, Jurassic, and Cretaceous formations. The Jurassic and Cretaceous strata have a later diagenetic age compared to rocks in eastern regions, resulting in relatively weaker cementation. The Jurassic strata consist mainly of sandstone, mudstone, and coal seams, while the Cretaceous strata are predominantly composed of conglomerate, gravelly sandstone, and mudstone. Currently, the mine is extracting coal from the #5 coal seam. The roof and floor of the coal seam are composed of siltstone and fine sandstone, respectively, with the main roof being fine sandstone. The porous and fractured aquifers of the Jurassic period are widely distributed across the mining area. The average distance between the top of the #5 coal seam and these aquifers is 23.47 m. As coal mining progresses and the overlying rock is damaged, these aquifers may become direct water-supplying aquifers for the #5 coal seam, posing a threat to the safety of coal mine production.

We observed the micro-pore structure characteristics of siltstone and sandstone under magnification levels ranging from 500x to 20,000x, as shown in Figure 1. At 1,000x magnification, the surface of the siltstone exhibits microcracks of varying scales. At 2,000x magnification, the particles and pores inside the cracks become visible. When the cracks are further magnified to 5,000x, a layered and flaky stacking structure can be observed on the surface. At 10,000x magnification, the arrangement of solid particles appears disordered, presenting a scattered state, which reflects poor cementation of the rock.

Similarly, after magnifying sandstone to 1,000x, pores of various sizes are visible on its surface. When these pores are magnified to 2,000x, it becomes evident that the cemented particles inside are not tightly bound and are not densely filled. At 5,000x magnification, the sandstone is mainly composed of fine particles that are less tightly cemented compared to siltstone. At 10,000x magnification, a certain amount of flocculent material can still be observed between the particles, with overall porosity remaining relatively high. Compared to siltstone, the sandstone exhibits poorer cementation of particles, a looser structure, and better connectivity between particles, resulting in a weakly cemented morphology.

2.2 Determination of physical similarity model parameters

Figure 1 shows that the overlying rock layer of the #5 coal seam at Yushuling Coal Mine exhibits weak cementation. The roof, with poor mechanical properties, is highly susceptible to deformation and failure under excavation disturbance, posing a significant safety risk to miners (Ju and Xu, 2015; Liu et al., 2022). To address this, we conducted a meter-scale physical model experiment to investigate the collapse of weakly cemented overburden and evolution of water-conducting fractures.

Based on the geological conditions of Yushuling Coal Mine and the similarity criteria for physical modeling, the geometric scale ratio of the experimental model was set at 100:1, with a density ratio (C_r) of 1.667:1. The dimensions of the physical model can thus be derived using the following formula (Gong et al., 2023):

$$C_l = \frac{l_i}{l_s} \tag{1}$$

where C_l is the geometric similarity ratio; l_i is the original size, m; l_s is the model size, m.

The motion similarity criterion is:

$$C_t = \frac{t_i}{t_s} = \sqrt{C_l} \tag{2}$$

where C_t is the similarity ratio of motion time; t_i is the original motion time, s; t_s is the model motion time, s.

The stress similarity criterion is:

$$C_p = \frac{p_i}{p_s} = C_r C_l \tag{3}$$

TABLE 1 Similar parameters of physical model.

Similarity parameter	Geometric similarity	Motion similarity	Stress similarity	Mass similarity
Symbol	C_l	C_t	C_p	C_m
Similarity ratio	100:1	10:1	167:1	167×10^6:1

where C_p is the stress similarity ratio; p_i is the original stress, Pa; p_s is the model stress, Pa.

The quality similarity criteria is:

$$C_m = \frac{m_i}{m_m} = C_r C_l^3 \tag{4}$$

Where C_m is the mass similarity ratio; m_i is the original mass, kg; m_m is the model mass, kg.

Table 1 summarizes the values of all similarity parameters in Equations 1–4. Laboratory and field measurement evidence indicates that the overburden of the coal seam is primarily subjected to compressive and tensile stresses, with failure manifesting as tensile-shear failure (Yu et al., 2023; Li et al., 2024). Therefore, the deformation and failure of the overburden during mining are related to the mechanical parameters of the rock layers, such as density, bulk modulus, shear modulus, and tensile strength. In order to faithfully replicate the actual geomechanical characteristics of the rock layers, we selected fine river sand with an average particle size of 0.25–0.35 mm as the granular material, and gypsum and calcium carbonate as the cementing materials. Additionally, mica powder was chosen to separate adjacent rock layers. The physical property parameters of the rock layers were primarily referenced from compressive and tensile strengths, and simulations were conducted by altering the composition ratio of the mixed materials. The mechanical property parameters of each rock layer in the similarity model are shown in Table 2. The material ratio parameters for each rock layer are shown in Table 3.

2.3 Experimental apparatus and procedure

We conducted the experiment using a self-constructed overburden displacement monitoring system (ODMS), the principle and components of which are shown in Figure 2. The experimental system primarily consists of the experimental platform, Match ID-2D analysis software, data acquisition system, speckle camera, and lighting system. The MatchID-2D non-contact full-field strain measurement system was used to monitor the displacement of the overburden during coal mining. The speckle camera was positioned at a specific angle to capture images of the model. A photo was taken each time a section of the coal seam was excavated, and another photo was taken half an hour after excavation was completed. Additional photos were taken whenever significant roof caving or noticeable widening of fractures occurred during mining. The images were sharpened and analyzed using the MatchID-2D analysis software to examine the speckle patterns.

The materials were weighed, mixed, laid, and compacted according to the ratio parameters listed in Table 3. Due to the shallow burial of the #5 coal seam at Yushuling Coal Mine, compensatory stress was not required to be applied above it. The overall model consists of 14 rock layers, with a final height of 135.7 cm, length of 250 cm, and a width of 30 cm upon completion. The model was allowed to air-dry naturally for 7–14 days before removing the front protective plate. A layer of white latex paint was applied to the surface, and uniform ink spots were marked on the paint to serve as displacement monitoring speckle.

To prevent boundary effects from affecting the accuracy of the experimental results, a 20 cm protective coal pillar was left at both ends of the #5 coal seam. These coal pillars effectively constrained the roof failure zone from extending beyond the boundaries on both sides of the model. In accordance with mining operation regulations, the working face is designed for a daily advancement of 3.2 m. Consequently, in the simulation of the mining process, the model was excavated by 3.2 cm at each step. To simulate the fully mechanized mining process, the excavation began with a 4 cm thick bottom coal layer, followed by excavation of the next bottom coal layer. After shifting the paper-based support frame, the previous step's 4.6 cm thick roof coal was excavated, with excavation occurring every half hour. As shown in Figure 2, three sets of pressure boxes, each containing five sensors, were arranged in the coal seam, immediate roof, and basic roof, totaling 15 sensors. They were positioned at distances of 20 cm, 40 cm, 60 cm, 100 cm, and 150 cm from the model boundary. The BZ2205C static strain measurement instrument was used to collect and record stress data.

2.4 Data interpretation

Digital speckle is a primary tool for measuring overburden movement. The calculation principle involves determining the deformation parameters of the physical model by analyzing the cross-correlation between the digital speckle fields before and after deformation (Xie et al., 2019; Mao et al., 2021), as illustrated in Figure 2. In the pre-deformation grayscale field, a sub-region O centered at the monitoring point P (x, y) is selected, with pixel dimensions of $M \times N$. When the surface of the measured object undergoes deformation, the sub-region O in the original grayscale field deforms into sub-region O', and its center point P (x, y) moves to $P'(x', y')$. At this point, the correlation coefficient between the two sub-regions, O and O', reaches its maximum value, enabling the calculation of the deformation value for the corresponding speckle points.

As shown in Figure 2, the rigid body displacement of point P (x, y) deformed to point and $P'(x', y')$ can be expressed as follows:

$$\begin{cases} x' = x + u(x,y) \\ y' = y + v(x,y) \end{cases} \tag{5}$$

TABLE 2 Similar simulation of mechanical property parameters of strata.

No.	Strata	Thickness (cm)	Tensile strength (MPa)	Compressive strength (MPa)	Simulated strength (KPa)
1	Coarse sandstone	36	1.49	53	317.37
2	Fine sandstone	7.4	1.46	38.91	232.99
3	Coarse sandstone	11.60	1.49	53	317.37
4	Glutenite	3	1.72	47.2	282.63
5	Fine sandstone	14.2	1.46	38.91	232.99
6	Siltstone	19.2	1.38	25	275.45
7	Fine sandstone	3.0	1.46	38.91	232.99
8	Siltstone	14	1.38	25	275.45
9	Siltstone	5.6	1.38	25	275.45
10	5# coal seam	8.6	0.78	23	137.72
11	Fine sandstone	8.0	1.46	38.91	232.99
12	Glutenite	3.6	1.72	47.2	282.63
13	Medium sand	1.5	1.53	28.56	171.02

TABLE 3 Similar simulation of material ratio parameters.

No.	Strata	Ratio no.	Total dry weight (kg)	Sand (kg)	Calcium carbonate (kg)	Gypsum (kg)	Thickness (cm)	Notes
1	Coarse sandstone	773	383.32	335.41	33.54	14.37	36	
2	Fine sandstone	437	83.22	66.58	4.99	11.65	7.40	
3	Coarse sandstone	773	131.39	114.96	11.5	4.93	11.60	
4	Glutenite	355	25.86	19.40	3.23	3.23	3.0	
5	Fine sandstone	437	148.71	118.95	8.93	20.83	14.20	
6	Siltstone	355	225.73	169.31	28.21	28.21	19.20	
7	Fine sandstone	437	34.64	27.71	2.08	4.85	3.0	
8	Siltstone	355	158.15	118.61	19.77	19.77	14	Immediate roof
9	Siltstone	537	60.74	50.61	3.04	7.09	5.60	Basic roof
10	5# coal seam	537	51.75	43.12	2.59	6.04	4.60	Top coal
11	5# coal seam	537	44.99	37.49	2.25	5.25	4.0	Bottom coal
12	Fine sandstone	437	93.54	74.82	5.62	13.10	8.0	
13	Glutenite	355	41.61	31.21	5.20	5.20	3.60	
14	Medium sand	637	16.87	14.46	0.72	1.69	1.50	
Sum			1500.52	1222.64	131.67	146.21		

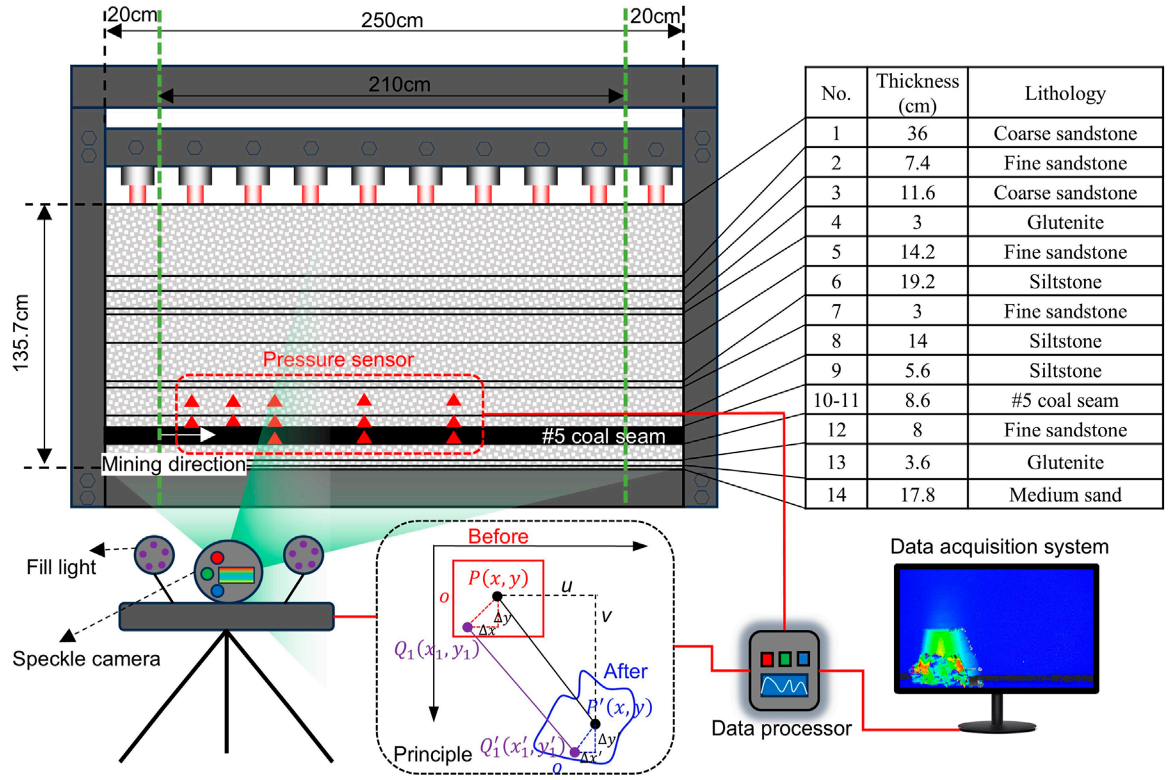

No.	Thickness (cm)	Lithology
1	36	Coarse sandstone
2	7.4	Fine sandstone
3	11.6	Coarse sandstone
4	3	Glutenite
5	14.2	Fine sandstone
6	19.2	Siltstone
7	3	Fine sandstone
8	14	Siltstone
9	5.6	Siltstone
10-11	8.6	#5 coal seam
12	8	Fine sandstone
13	3.6	Glutenite
14	17.8	Medium sand

FIGURE 2
Principle and main components of the overburden displacement monitoring system (ODMS).

Where $u(x,y)$ and $v(x,y)$ are the displacement components of the midpoint of the sub region in the X and Y directions before and after deformation, respectively.

In addition to the rigid body displacement of the center point, the measured area will also produce deformation. Any point Q $(x_1+\Delta x,\ y_1+\Delta_y)$ in the sub region before deformation becomes $Q'(x_1'+\Delta x',\ y_1'+\Delta y')$ after deformation, and $\Delta x'$ and $\Delta y'$ are:

$$\begin{cases} \Delta x' = \Delta x + \Delta u(x,y) \\ \Delta y' = \Delta y + \Delta v(x,y) \end{cases} \tag{6}$$

Where Δx and Δy are the distances between the point Q before deformation and the center point P in X and Y directions respectively, and $\Delta x'$ and $\Delta y'$ are the distances between Q' and the center point P' after deformation in X and Y directions respectively. Where Δu and Δv can be expressed as:

$$\begin{cases} \Delta u(x,y) = \dfrac{\partial u(x,y)}{\partial x}\Delta x + \dfrac{\partial u(x,y)}{\partial y}\Delta y \\ \Delta v(x,y) = \dfrac{\partial v(x,y)}{\partial x}\Delta x + \dfrac{\partial v(x,y)}{\partial y}\Delta y \end{cases} \tag{7}$$

The deformation displacement can be obtained by combining Equations 5–7:

$$\begin{cases} x' + \Delta x' = x + u + \left\{1 + \dfrac{\partial u(x,y)}{\partial x}\right\}\Delta x + \dfrac{\partial u(x,y)}{\partial y}\Delta y \\ y' + \Delta y' = y + v + \left\{1 + \dfrac{\partial v(x,y)}{\partial x}\right\}\Delta x + \dfrac{\partial v(x,y)}{\partial y}\Delta y \end{cases} \tag{8}$$

From Equation 8, it can be seen that after the measured object undergoes deformation, the displacement deformation of any point within the subregion can be represented by the displacement $u(x,y)$, $v(x,y)$ and its derivatives.

When solving for the displacement of monitoring points, we use the normalized sum of squared differences (NSSD) function to track the positional changes of each scattered spot. The sub-regions before and after deformation can be determined using Equation 9 (Mao et al., 2021):

$$C_{NSSD} = \sum_{x=-M}^{M}\sum_{y=-M}^{M}\left[\frac{f(x,y)}{\sqrt{\sum_{x=-M}^{M}\sum_{y=-M}^{M} f(x,y)^2}} - \frac{g(x',y')}{\sqrt{\sum_{x=-M}^{M}\sum_{y=-M}^{M} g(x',y')^2}}\right]^2 \tag{9}$$

Where $f(x,y)$ and $g(x',y')$ are the grayscale of the central point of the sub region before and after deformation respectively.

3 Results and discussion

3.1 Movement and displacement characteristics of overburden

We observed periodic collapses of the overlying rock after the completion of the 16th and 22nd excavation stages, as

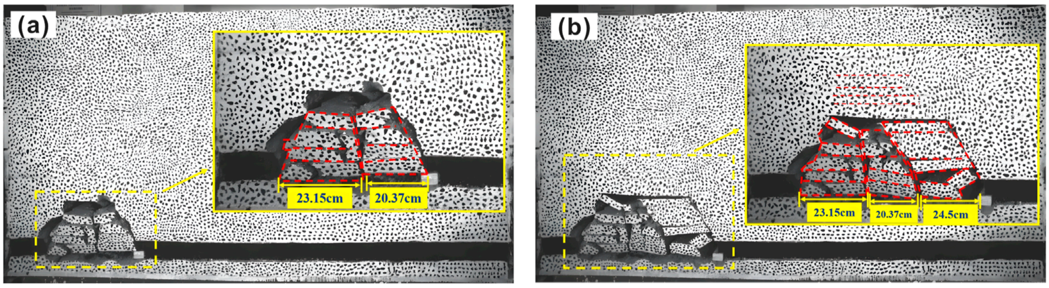

FIGURE 3
The collapse step distance of the overlying rock following the **(A)** 16th and **(B)** 22nd excavations.

indicated by snapshot images. The failure phenomena following these stages are shown in Figure 3. After the 16th excavation, the simulated working face advanced by 51.2 cm, causing periodic collapses of the overlying rock with step distances of 23.15 cm and 20.37 cm, respectively. Following the 22nd excavation, the third periodic collapse occurred, with the working face advancing by approximately 70.4 cm. This event led to new collapses in the main roof and the formation of horizontal fractures in the overlying rock, with a collapse step distance of 24.5 cm. Consequently, periodic collapses occurred roughly every 20 cm of advancement.

Figure 4 presents variation cloud maps of vertical displacement for both the basic roof and the weakly cemented key layer, along with vertical displacement curves for each measurement line in the direction of advancement. Figure 4A shows that, during the advancement of the working face (A_d) by 30–50 cm, the immediate roof experienced three collapses: the first, caused by simulated blasting to cut the roof, and the second and third. as natural collapses of the immediate roof. The first collapse of the basic roof occurred when the working face advanced to 70 cm, with a collapse height of approximately 18 cm. During the advancement of the working face to 90 cm, two large-scale collapses of the overburden occurred. When the working face reached 90 cm, the maximum height of the overburden cracks was approximately 40 cm above the coal seam. Additionally, when the working face advanced to 100 cm, a break occurred in the weakly cemented key layer, causing the overburden to collapse as well, with a collapse height of approximately 85 cm. As the working face advanced to 130 cm, a 3.7 cm-thick coarse sandstone layer fractured. At 135 cm, the basic roof underwent rotational instability. When the working face reached 140 cm, a slight penetrating fracture developed in the weakly cemented key layer. By 160 cm, fractures in the overburden above the coal seam had further developed, and fractures in the weakly cemented key layer propagated upward to the surface.

As shown in Figure 4B, the basic roof's maximum vertical displacement during advancement distances (A_d) of 30 cm, 50 cm, 70 cm, and 90 cm was 0.19 mm, 0.33 mm, 2.57 mm, and 65.4 mm, respectively. The maximum subsidence occurred primarily within the advancement range of 516 mm–630 mm. According to Figure 4C, the corresponding maximum vertical displacements at these advancement distances were 0.26 mm, 0.33 mm, 1.55 mm, and 52.3 mm, with the maximum subsidence occurring between 510 mm and 650 mm. At 90 cm, the vertical displacement differed by 13.1 mm between the two measurements.

Figure 4D shows the vertical displacement at Measurement Line one of the weakly cemented key layer at advancement distances of 30 mm, 50 mm, 70 mm, 90 mm, 110 cm, 130 cm, 150 cm, and 160 cm, which were 0.3 mm, 0.7 mm, 1.2 mm, 7.3 mm, 80 mm, 88 mm, 92 mm, and 90 mm, respectively. The maximum vertical displacement occurred primarily between 590 mm and 660 mm. Notably, at the 125 cm advancement point, a smaller peak is observed due to the rotation of the weakly cemented key layer.

As shown in Figure 4E, the maximum vertical displacements of the weakly cemented key layer at various advancement distances were 0.3 mm, 0.3 mm, 0.9 mm, 5.08 mm, 71 mm, 80 mm, 83 mm, and 83 mm, respectively. The maximum vertical displacements mainly occurred between 530 mm and 730 mm. During the advancement from 30 mm to 90 mm, the average maximum vertical displacement of the weakly cemented key layer was 6.19 mm, indicating that the weakly cemented key layer remained largely intact and stable. When the working face reached 160 cm, the average maximum vertical displacement increased to 86.5 mm. In other words, as the working face advanced to 160 m, the weakly cemented key layer at the Yushuling Coal Mine subsided by approximately 8.65 m.

3.2 Characteristics of overburden failure and water-conducting fractures

The top-coal mining was simulated based on the actual conditions of the mine, with each excavation advancing by 3.2 cm. In the first three steps, only 4 cm of bottom coal was extracted. After the fourth excavation, the top coal from the first three steps was simultaneously released, simulating the actual blasting and cutting of the roof. Figure 5A illustrates the collapse process of the immediate roof during excavation., The first collapse of the immediate roof occurred during the sixth excavation followed by a second collapse after the 10th excavation. Throughout this process, no fractures developed in the overlying rock above the immediate roof. During the 17th excavation, horizontal fractures in the main roof widened, and vertical fractures began to form. After the second collapse of the immediate roof, a longitudinal fracture developed in the central part of the main roof. However, this fracture had not

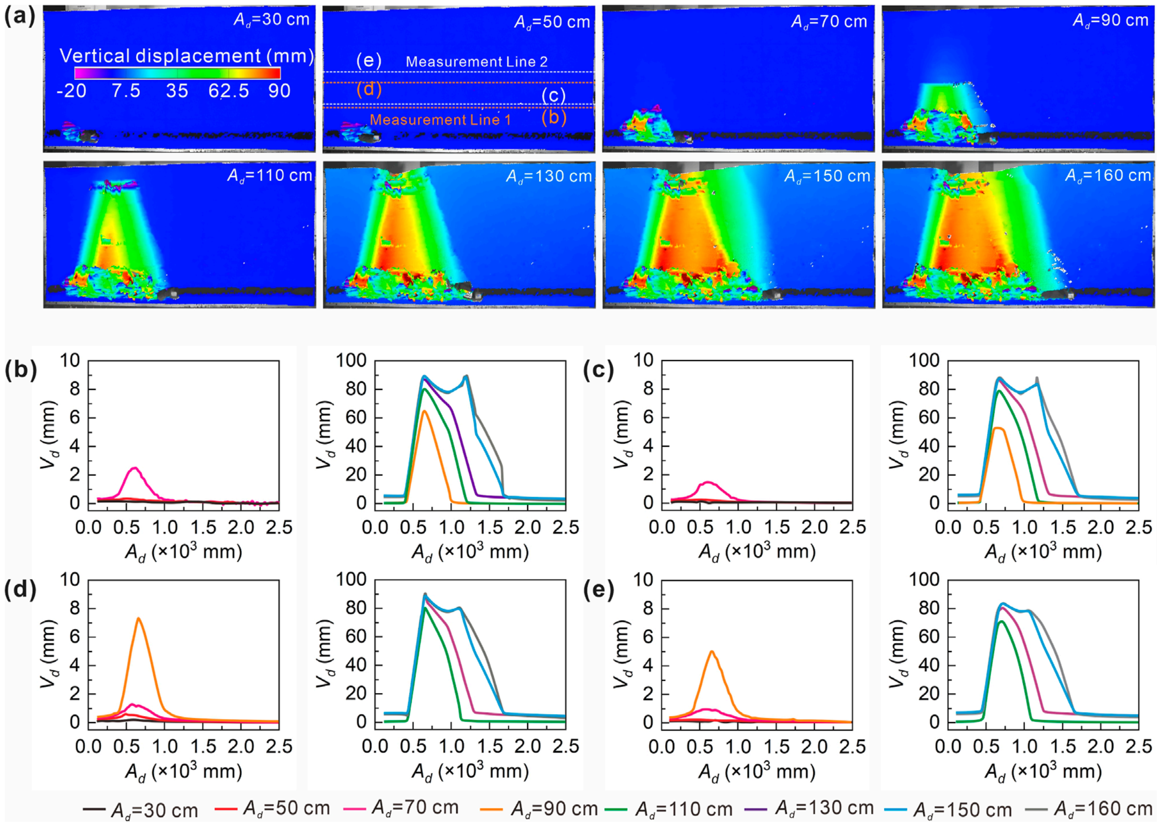

FIGURE 4
(A) Evolution of the nephogram for vertical displacement of the rock stratum at different working face advance distances (A_d). Vertical displacement curves for **(B)** Measurement Line one and **(C)** Measurement Line two of the basic top along the advance distance (A_d). Vertical displacement curves for **(D)** Measurement Line one and **(E)** Measurement Line two of the weakly cemented key layer along the advance distance (A_d).

yet penetrated the main roof, and no water-conducting fractures were formed.

The failure process of the main roof is shown in Figure 5B. After the 17th coal release and support removal, the main roof collapsed for the first time, reaching a height of approximately 14.5 cm above the coal seam. Some of the collapsed rock layers developed fractures. Following the 22nd excavation, both the main roof and the overlying rock layers developed a fracture that extended approximately 35.5 cm above the top coal. As the rock layers underwent overall downward rotation, a longitudinal through fracture formed in the main roof. During the 25th excavation, pressure from the overlying rock layers caused the immediate roof to make contact with the floor of the working face. The fractures between the overlying main roof and the underlying rock layers closed, while the separation between the main roof and the weakly cemented critical layer increased, causing the interlayer fractures in the upper rock layers to widen.

The four collapse processes of the overlying rock of the weakly cemented critical layer during the 39th to 60th excavation stages are shown in Figure 5C. After the 39th coal release, fractures continued to propagate upward toward the surface. Following the 43rd excavation, the main roof and overlying rock layers rotated and subsided. As a result, the fractures in the overlying rock widened further, and a longitudinal fracture extending to the surface formed. After the 60th coal release, the immediate roof became unstable and collapsed, triggering a third periodic collapse of the overlying rock. At this point, the model was near the reserved protective coal pillar, and the fractures in the overlying rock ceased to develop.

3.3 Stress evolution of weakly cemented overburden at the engineering scale

To clearly characterize the collapse features of weakly cemented overburden in the Yushuling Coal Mine, we developed an engineering-scale numerical model using the FLAC3D software package. FLAC3D is widely applied across various fields, including mining engineering, civil engineering, and materials science (Li W. et al., 2022; Zhu Z. et al., 2022; Teng et al., 2023). The reliability of its numerical simulations has been validated through experimental data and analytical solutions (Wang G. et al., 2021).

The Mohr-Coulomb criterion, recognized for its exceptional reliability, was selected to model the deformation behavior of the overburden at the Yushuling Coal Mine. Boundary conditions include fixed horizontal displacements on the sides, fixed vertical displacements at the bottom, and a free boundary at the top. No additional constraints are applied, and the effects of initial joint fractures in the bedding layers are not considered. Table 4

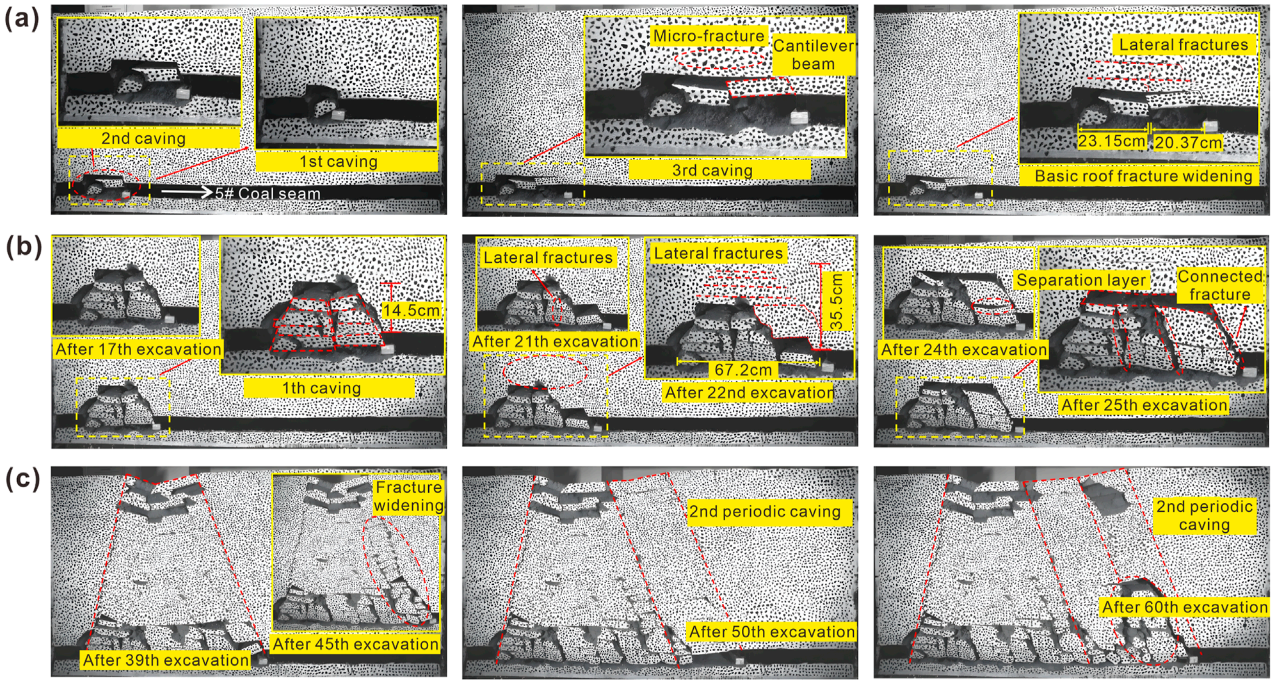

FIGURE 5
Formation process of strata caving and water-conducting fractures process. **(A)** Direct roof. **(B)** Basic roof. **(C)** Overburden of weakly cemented key layer.

TABLE 4 Numerical model rock formation parameters.

No.	Strata	Thickness (m)	Density (kg/m^3)	Bulk modulus (MPa)	Shear modulus (MPa)	Tensile strength (MPa)	Angle of internal friction (°)
1	Coarse sandstone	36	2,490	2,679	1764	1.49	43.15
2	Fine sandstone	7.40	2,630	2,643	1820	1.46	40.23
3	Coarse sandstone	11.60	2,490	2,679	1764	1.49	43.15
4	Glutenite	3	2,540	2,886	1901	1.72	39.60
5	Fine sandstone	14.20	2,630	2,643	1820	1.46	40.23
6	Siltstone	19.20	2,660	3,550	2,345	1.38	39.60
7	Fine sandstone	3	2,630	2,643	1820	1.46	40.23
8	Siltstone	14	2,660	3,550	2,345	1.38	39.60
9	Siltstone	5.60	2,660	3,550	2,345	1.38	39.60
10	#5 coal seam	8.80	1350	2,139	1204	0.78	48.23
11	Fine sandstone	8	2,630	2,643	1820	1.46	40.23
12	Glutenite	3.60	2,540	2,886	1901	1.72	39.60
13	Medium sand	17.80	2,630	2,643	1820	1.46	40.23

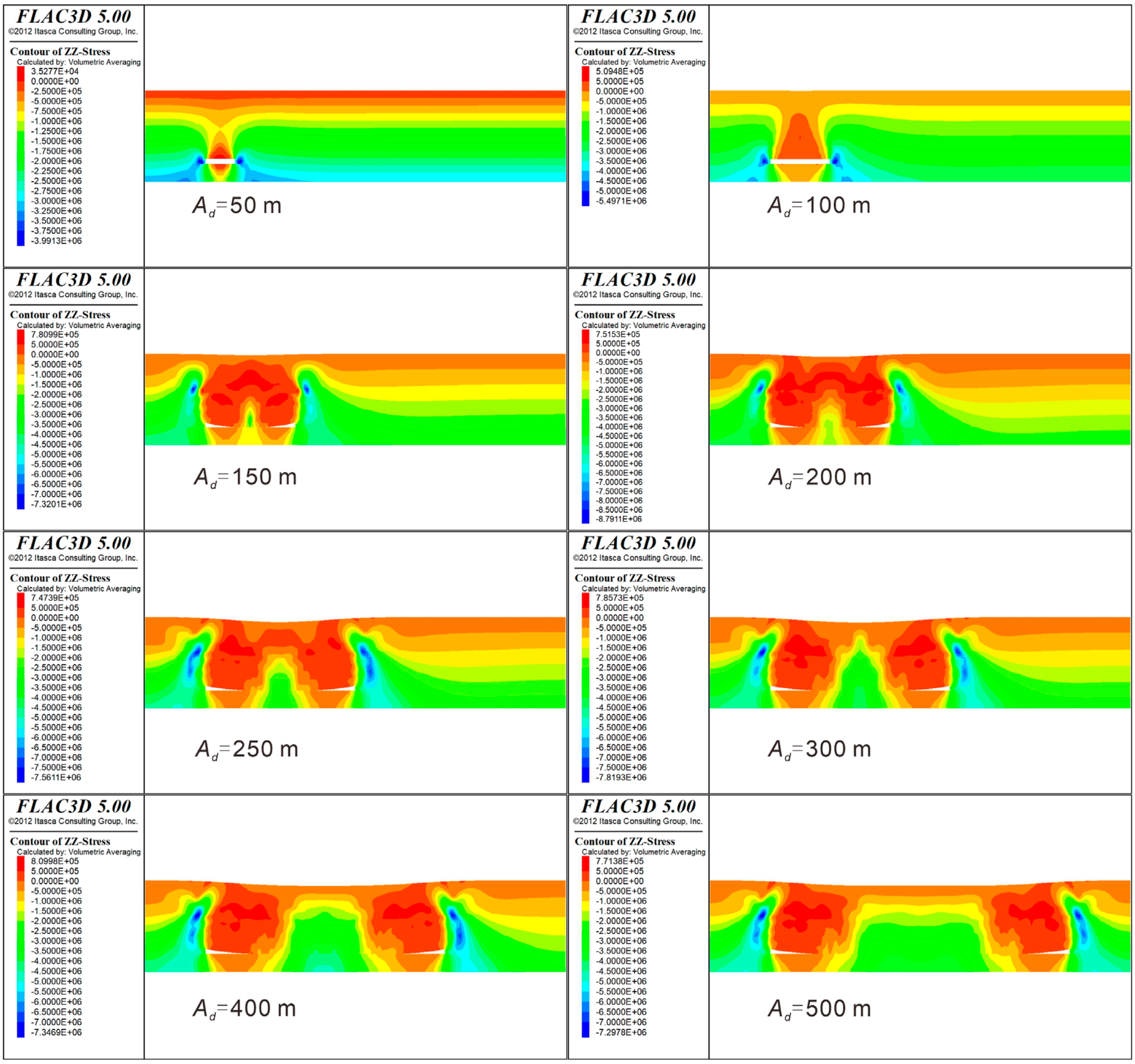

FIGURE 6
Vertical stress distribution of strata at varying advancing distances of the working face.

presents the input parameters for the numerical model. Further details on the modeling process can be found in our earlier work (Liu et al., 2023).

The deformation pattern of the overburden can be obtained by inputting the mining plan of the Yushuling Coal Mine into FLAC3D. In the numerical model, excavation begins sequentially with the transport entry, the outer section of the return air roadway, and the old cutting face. After equilibrium is achieved, excavation progresses with the new cutting face, the inner section of the return air roadway, and the modified tunnel, with equilibrium being reestablished after each step. Once the mining roadway excavation is completed, the working face advances from 0 m to 65 m. It is then extended to 155 m and continues forward until reaching the old cutting face. Beyond this point, excavation proceeds for an additional 460 m until the protective coal pillar is encountered.

3.3.1 Variation characteristics of overburden stress

The vertical stress distribution of the overburden at various stages of the working face advance (50 m, 100 m, 150 m, 200 m, 250 m, 300 m, 400 m, and 500 m) is shown in Figure 6. As the working face progresses, the stress field of the overburden continuously changes. After coal seam extraction, stress in the overburden redistributes. When the overburden exceeds its bearing capacity, it fractures, generating mining-induced fractures and creating a symmetrical stress field similar to the plastic zone that forms above the goaf. In addition, stress concentration zones are formed on both sides of the goaf, which can easily develop into water-conducting fractures.

When the working face advances to 50 m, small, symmetrical pressure-relief arches form above and below the goaf, indicating

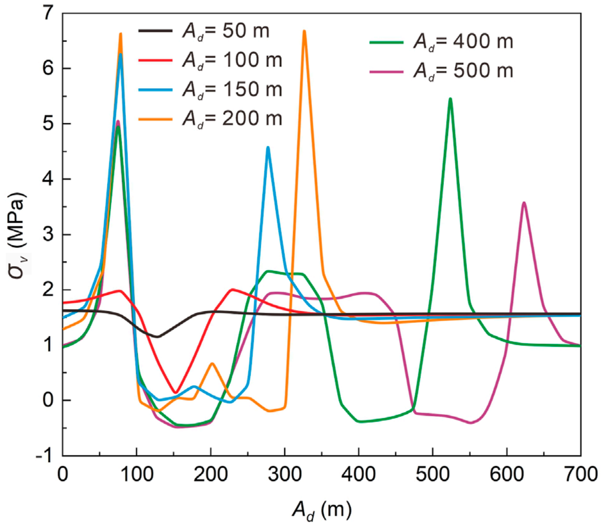

FIGURE 7
The distribution of vertical stress in weakly cemented siltstone (No. 6 in Table 4) along the advancing direction.

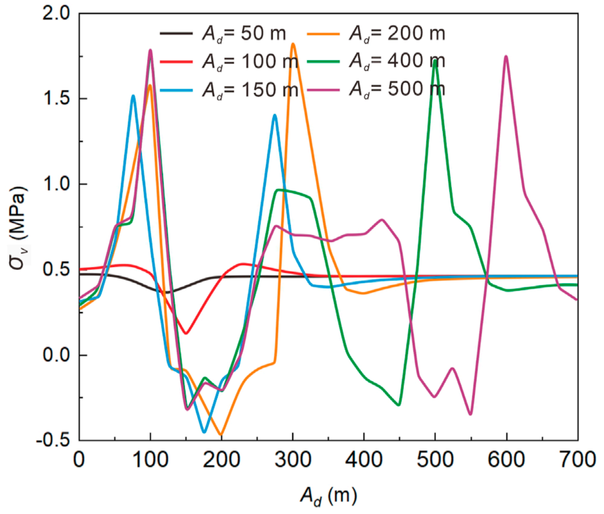

FIGURE 8
The distribution of vertical stress in ground coarse sandstone (No. 1 in Table 4) along the advancing direction.

the development of fractures in the overburden. At this point, the maximum stress is approximately 4 MPa, with a stress concentration factor of 1.3. As the working face progresses to 100 m, the pressure-relief zone above the goaf extends upward, causing the immediate roof to collapse, and the stress concentration on both sides of the goaf to decrease. At 200 m, the pressure-relief arch in the overburden is symmetrically distributed around the center of the goaf, with stress release further extending upward and the stress concentration zone shifting upwards. Beyond 200 m, the height of the overburden fractures remains relatively unchanged, while the maximum stress above the mining area increases with the advance of the working face. Notably, when the working face reaches 400 m and 500 m, the overburden fractures on both sides of the goaf become more extensive, and the degree of damage intensifies. This suggests that the overlying aquifer can reach the goaf through fractures above both sides of the goaf.

Variation data of vertical stress along the advancing direction at the middle position of the 19.2 m thick weakly cemented siltstone (as shown in Figure 7) and the 36 m thick coarse sandstone (as shown in Figure 8) were obtained using the FISH language. Figure 7 shows that when the working face advanced to 50 m, the variation in vertical stress in the goaf area was minimal. The stress contour map revealed that the overlying strata had not collapsed at this stage. When the working face advanced to 100 m, fine fractures developed in the weakly cemented critical layer, and slight stress concentration appeared on both sides of the goaf. When the working face advanced 400 m and 500 m, the vertical stress in the stress concentration area of the weakly cemented siltstone critical layer decreased compared to previous values. In the final state, the vertical stress at the ends of the goaf were minimal, indicating that fractures were more pronounced at these locations than elsewhere.

Figure 8 shows that when the advancing distance is small, the variation in vertical stress resembles that at the position of the weakly cemented key layer (Figure 7), but the stress change is not significant, indicating that no failure in this layer. However, when the working face advances to the 150 m position, a stress reduction zone appears at the corresponding location in the middle of the goaf, while stress concentration is observed near the coal pillars on both sides of the goaf The maximum vertical stress reaches 1.5 MPa, with a stress concentration factor of 0.5, indicating a slight surface bending in the central region of the goaf. As the working face advances further to 200 m, the vertical stress increases to 1.9 MPa, and the stress concentration factor becomes 0.6. Beyond 400 m, the vertical stress is relatively low, indicating that fewer fractures have formed at the surface compared to the position of the weakly cemented key layer.

3.3.2 Variation characteristics of overburden displacement

During the mining process, as the working face advances, the overlying strata experience varying degrees of movement and subsidence, indirectly reflecting the development patterns of the water-conducting fracture zone.

Figure 9 shows the contour map of vertical displacement in the overburden during the advancement of the working face. When the working face advances less than 100 m, the displacement contour map of the overburden above the mined area shows an arch-shaped distribution, symmetrically centered along the mined area. The maximum vertical displacements are 242 mm and 811 mm, indicating roof delamination. When the working face reaches 150 m, mining-induced disturbances increase, causing further displacement in the overburden above the mined area. The maximum displacement extends beneath the weakly cemented key layer, reaching 8.86 m, suggesting significant fracture development. By the time the working face reaches 200 m, the maximum vertical displacement of the overburden increases slightly to 8.89 m. At this point, the overburden is essentially fully mined, with minimal increase in fractures.

After the working face advances beyond 200 m, the vertical displacement of the overburden shows little change. Based on the

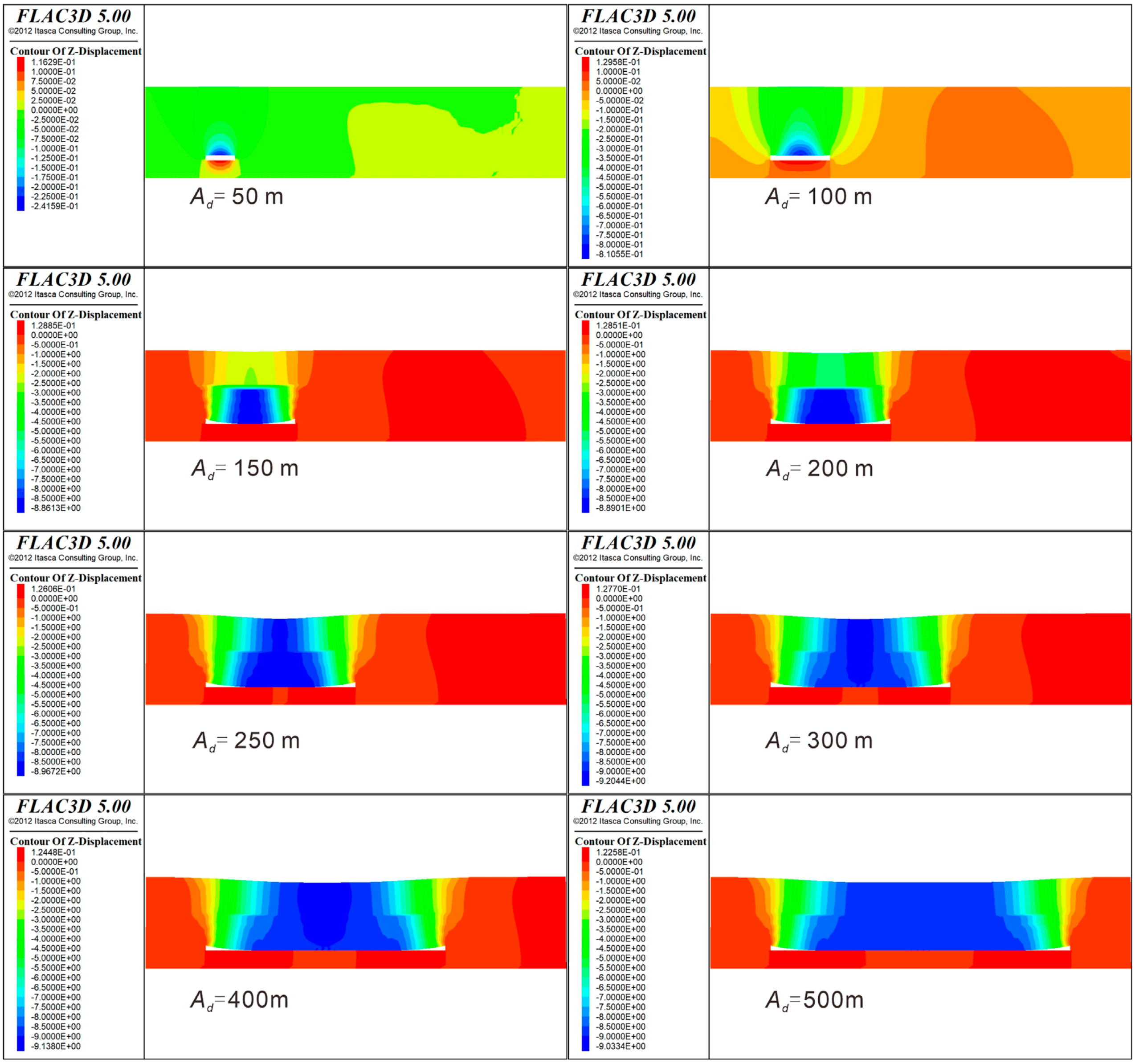

FIGURE 9
Vertical displacement of strata at varying advancing distances of the working face.

stress variations, it is evident that the height of fracture development no longer increases significantly with further advancement of the working face. When the working face exceeds 300 m, the maximum vertical displacement also levels off, while the subsidence area of the overburden continues to expand. This indicates that the overburden has reached a fully mined state, the mined area has compacted, and the height of the water-conducting fracture zone has stabilized.

To provide a clearer depiction of the overlying rock's behavior during the mining process, Figure 10 illustrates the vertical displacement distribution at the surface along the direction of advancement. As shown, during the first 100 m of advancement, there is minimal displacement of the overlying rock at the surface. When the working face advanced to 150 m from the starting point, significant displacement occur at the weakly cemented key layer, causing the surface to subsided by approximately 2.5 m. At 200 m, the subsidence increases to around 5.3 m. Between 250 m and 500 m, the maximum vertical displacement reaches its peak, ranging from approximately 8.9–9 m. Beyond 500 m, the vertical displacement stabilizes, and a flat-bottom section forms, halting further surface subsidence.

4 Conclusion

We conducted a study using a meter-scale experimental approach and a site-scale numerical model to investigate the deformation and failure evolution of shallowly buried, weakly cemented overburden, as well as the formation and evolution of

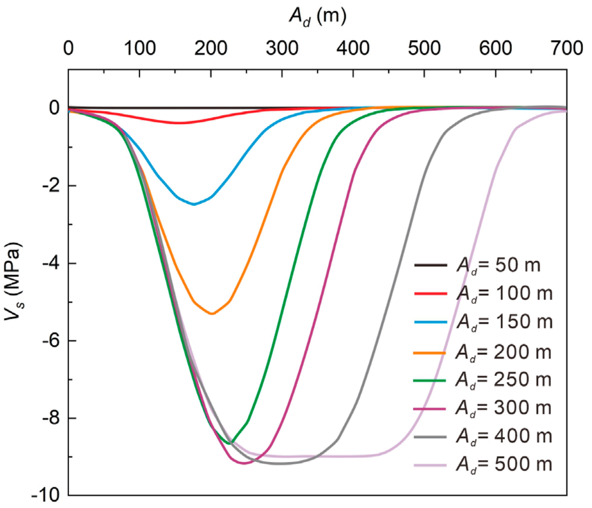

FIGURE 10
Vertical displacement curves of the mode surface.

water-conducting fractures. Based on these analyses, the following key conclusions were drawn:

(1) The breaking distance of the model overburden was determined to be 20 m. At a 160 m advancement, the maximum vertical displacements of the basic roof and the weakly cemented key layer were 8.9 m and 8.65 m, respectively. The overburden above the weakly cemented key layer collapsed as the key layer fractured, with a maximum vertical displacement of 8.2 m.
(2) During excavation, the step distances for the collapse of the immediate roof and the basic roof were found to be 22 m and 22.4 m, respectively. After the fracture of the weakly cemented key layer, the overlying rock layers also collapsed, with a maximum collapse height of 96.3 m. This indicates that the actual water-conducting fracture zone extended to a height of 96.3 m. Additionally, at the end of the model mining process, the overburden underwent four cycles of periodic collapse.
(3) Following mining at the working face, the overburden in the center of the goaf became compacted, while the overburden on both sides of the goaf exhibited stress concentration, forming a stress field with higher values at the ends and lower values in the middle. During the first 200 m of advancement, fractures developed below the weakly cemented key layer. However, between the 200 m–500 m advancements, fractures extended to the surface, and the overburden collapse reached a fully developed state, with the height of the water-conducting fracture zone stabilizing.
(4) The maximum vertical stress in the weakly cemented key layer during the advancement process was 6.7 MPa, with a stress concentration factor of 2.2. The maximum vertical stress in the surface coarse sandstone was 1.9 MPa, with a stress concentration factor of 0.6. When the working face advanced to approximately 200 m, the overburden had essentially reached a fully mined state.

Data availability statement

The original contributions presented in the study are included in the article/supplementary material, further inquiries can be directed to the corresponding authors.

Author contributions

ZL: Conceptualization, Investigation, Supervision, Writing–original draft. YZ: Conceptualization, Formal Analysis, Methodology, Writing–original draft. XG: Investigation, Writing–original draft, Writing–review and editing, Formal Analysis. DM: Conceptualization, Funding acquisition, Project administration, Writing–review and editing. LF: Formal Analysis, Writing–review and editing. GL: Data curation, Software, Writing–review and editing. XL: Validation, Visualization, Writing–review and editing. MH: Resources, Validation, Writing–original draft. ZC: Software, Visualization, Writing–original draft.

Funding

The author(s) declare that financial support was received for the research, authorship, and/or publication of this article. This research was funded by the National Natural Science Foundation of China (U23B2091, U24B2041, 52404157 and 52174073), the National Key R&D Program of China (2022YFC2905600) and the program for the scientific and technological innovation team in universities of Henan province (23IRTSTHN005).

Conflict of interest

Author YZ was employed by Shenhua New Street Energy Co., Ltd. Author GL was employed by Jiaozuo Coal Group Co., Ltd. Author MH was employed by Xinqiao Coal Mine of Yongmei Group Co., Ltd. Author XL was employed by Jiaozuo Coal Industry (Group) Xinxiang Energy Co., Ltd. Author ZC was employed by Zhengzhou Coal Industry (Group) Yanghe Coal Industry Co., Ltd.

The remaining authors declare that the research was conducted in the absence of any commercial or financial relationships that could be construed as a potential conflict of interest.

Generative AI statement

The authors declare that no Generative AI was used in the creation of this manuscript.

Publisher's note

References

Di, S. (2022). Predicting overburden-induced failure height of large mining face in shallow coal seam based on half-plane theory. *Shock Vib.* 2022 (1), 1–10. doi:10.1155/2022/5757871

Dong, F., Yin, H., Ren, H., Cheng, W., Tai, S., Miao, T., et al. (2024). Trapezoidal failure behavior and fracture evolution mechanism of overburden in extra-thick coal mining in weakly cemented strata. *Rock Mech. Rock Eng.* 57, 11239–11260. doi:10.1007/s00603-024-04147-3

Gong, Y.-F., Zhu, C.-Y., and Zhu, G.-W. (2023). Analysis of physical parameters of materials similar to coal and rock mass based on geophysical model construction of mines. *Appl. Geophys.* 20 (1), 116–129. doi:10.1007/s11770-022-0957-z

Ju, J., and Xu, J. (2015). Surface stepped subsidence related to top-coal caving longwall mining of extremely thick coal seam under shallow cover. *Int. J. Rock Mech. Min.* 78 (0), 27–35. doi:10.1016/j.ijrmms.2015.05.003

Li, A., Ding, X., Yu, Z., Wang, M., Mu, Q., Dai, Z., et al. (2022a). Prediction model of fracture depth and water inrush risk zoning in deep mining coal seam floor. *Environ. Earth Sci.* 81 (11), 315. doi:10.1007/s12665-022-10431-8

Li, S., Gao, M., Yang, X., Zhang, R., Ren, L., Zhang, Z., et al. (2018). Numerical simulation of spatial distributions of mining-induced stress and fracture fields for three coal mining layouts. *J. Rock Mech. Geotech. Eng.* 10 (5), 907–913. doi:10.1016/j.jrmge.2018.02.008

Li, T., Duan, Z., He, H., and Song, H. (2023). Study on the carrying capacity and change trend of groundwater resources in coal mining area: a case study of a coal mine in northwest China. *Water* 15 (1551), 1551. doi:10.3390/w15081551

Li, W., Wu, W., and Zhang, J. (2022b). Numerical stability analysis of the dam foundation under complex geological conditions at great depth: a case study of kala hydropower station, China. *Front. Phys-Lausanne* 9. doi:10.3389/fphy.2021.808840

Li, W.-t., Wang, L.-y., Zhang, C.-a., Yang, X.-z., Mei, Y.-c., Shao, X., et al. (2024). Numerical investigation study on tensile-shear failure behavior of rock bolts in inclined strata mining tunnels. *Eng. Fail. Anal.* 162, 108393. doi:10.1016/j.engfailanal.2024.108393

Liu, G., Zou, Y., Zhang, W., and Chen, J. (2022). Characteristics of overburden and ground failure in mining of shallow buried thick coal seams under thick aeolian sand. *Sustainability* 14 (4028), 4028. doi:10.3390/su14074028

Liu, Q., Zhou, C., Ma, D., Liu, Y., Wang, G., and Huang, Z. (2023). Evolution of water-conducting fracture in weakly cemented strata in response to mining activity: insights from experimental investigation and numerical simulation. *Water* 15 (23), 4173. doi:10.3390/w15234173

Liu, X., Zeng, Y., Wu, Q., Meng, S., Liang, J., and Hou, Z. (2024). Ecological-based mining: a coal-water-thermal collaborative paradigm in ecologically fragile areas in western China. *Engineering* 38 (7), 209–222. doi:10.1016/j.eng.2024.01.019

Ma, D., Duan, H., Li, Q., Wu, J., Zhong, W., and Huang, Z. (2023). Water–rock two-phase flow model for water inrush and instability of fault rocks during mine tunnelling. *Int. J. Coal Sci. Techn.* 10 (1), 77–19. doi:10.1007/s40789-023-00612-6

Ma, D., Duan, H., Zhang, J., and Bai, H. (2022). A state-of-the-art review on rock seepage mechanism of water inrush disaster in coal mines. *Int. J. Coal Sci. Techn.* 9 (1), 50–28. doi:10.1007/s40789-022-00525-w

Mao, L., Liu, H., Wang, Y., Ding, L., Ju, Y., and Chiang, F.-P. (2021). 3-D strain estimation in sandstone using improved digital volumetric speckle photography algorithm. *Int. J. Rock Mech. Min.* 141, 104736. doi:10.1016/j.ijrmms.2021.104736

Meng, L., Han, L., Zhu, H., Dong, W., and Li, W. (2021). Influence of moisture content on the structural characteristics of argillaceous weakly consolidated rock caused by dynamic loading in the coal mine. *Shock Vib.* 2021. doi:10.1155/2021/7206801

Teng, F., Yu, M., Yu, M., Han, X., and Chao, J. (2023). Study on the mechanism of coal pillar breaking and fracture development under repeated mining in a close seam group. *Front. Earth Sc-Switz* 10, 991304. doi:10.3389/feart.2022.991304

Wang, G., Li, P., Wu, Q., Cui, X., and Tan, Z. (2021a). Numerical simulation of mining-induced damage in adjacent tunnels based on FLAC^{D}. *Adv. Civ. Eng.* 2021 (5), 9855061–9855021. doi:10.1155/2021/9855067

Wang, H., Yang, T., and Zuo, Y. (2018). Experimental study on acoustic emission of weakly cemented sandstone considering bedding angle. *Shock Vib.* 2018 (Part 6), 6086581–6086512. doi:10.1155/2018/6086583

Wang, X., Zhu, S., Yu, H., and Liu, Y. (2021b). Comprehensive analysis control effect of faults on the height of fractured water-conducting zone in longwall mining. *Nat. Hazards* 108 (2), 2143–2165. doi:10.1007/s11069-021-04772-z

Wu, J., Wong, H. S., Zhang, H., Yin, Q., Jing, H., and Ma, D. (2024). Improvement of cemented rockfill by premixing low-alkalinity activator and fly ash for recycling gangue and partially replacing cement. *Cem. Concr. Comp.* 145 (0), 105345. doi:10.1016/j.cemconcomp.2023.105345

Xie, Z., Zhang, N., Meng, F., Han, C., An, Y., and Zhu, R. (2019). Deformation field evolution and failure mechanisms of coal–rock combination based on the digital speckle correlation method. *Energies* 12 (13), 2511–2514. doi:10.3390/en12132511

Xu, H., Lai, X., Zhang, S., Zhang, Y., Shan, P., Zhang, X., et al. (2021). Multiscale intelligent inversion of water-conducting fractured zone in coal mine based on elastic modulus calibration rate response and its application: a case study of ningdong mining area. *Lithosphere* 2021 (4), 7657143. doi:10.2113/2021/7657143

Yan, M., Deng, J., Yu, B., Li, M., Zhang, B., Xiao, Q., et al. (2020). Comparative study on sanding characteristics between weakly consolidated sandstones and unconsolidated sandstones. *J. Nat. Gas. Sci. Eng.* 76 (0), 103183. doi:10.1016/j.jngse.2020.103183

Yang, W., and Xia, X. (2018). Study on mining failure law of the weak and weathered composite roof in a thin bedrock working face. *J. Geophys. Eng.* 15 (6), 2370–2377. doi:10.1088/1742-2140/aacedf

Yu, J., Yu, J., Zhou, Z., Liu, H., Zhou, L., Li, Z., et al. (2023). Experimental study on the shear failure of layered rock bridges. *Front. Earth Sc-Switz* 11, 1209259. doi:10.3389/feart.2023.1209259

Zha, H., Liu, W., and Liu, Q. (2020). Physical simulation of the water-conducting fracture zone of weak roofs in shallow seam mining based on a self-designed hydromechanical coupling experiment system. *Geofluids* 2020 (0), 1–14. doi:10.1155/2020/2586349

Zhang, C., Wang, P., Wang, E., Chen, D., and Li, C. (2023a). Characteristics of coal resources in China and statistical analysis and preventive measures for coal mine accidents. *Int. J. Coal Sci. Techn.* 10 (2), 22–57. doi:10.1007/s40789-023-00582-9

Zhang, G., Guo, G., Lv, Y. N., and Gong, Y. (2020). Study on the strata movement rule of the ultrathick and weak cementation overburden in deep mining by similar material simulation: a case study in China. *Math. Probl. Eng.* 2020 (1), 1–21. doi:10.1155/2020/7356740

Zhang, G., Guo, G., Wei, W., Wang, J., Li, H., and Du, Q. (2022a). Mechanical properties and failure mechanism of the weakly cemented overburden in deep mining. *Minerals* 12 (1276), 1276. doi:10.3390/min12101276

Zhang, J., Wu, J., Yang, S., and Bai, W. (2022b). Analysis and control of the mechanism of coal pillar sloughing in the shallow buried thick coal seam. *Energy Sci. Eng.* 10 (10), 3692–3710. doi:10.1002/ese3.1269

Zhang, L., Zhang, Z., Wang, K., Tan, X., Zhang, T., and Zhang, L. (2023b). Characteristic developments of the water-conducting fracture zones in weakly cemented overlying strata of jurassic coal mines in western China. *Water* 15 (6), 1097. doi:10.3390/w15061097

Zhang, S., Fan, G., Zhang, D., Luo, T., Guo, X., Dun, S., et al. (2022c). Physical simulation on weakly cemented aquiclude stability due to underground coal mining. *Minerals* 12 (1494), 1494. doi:10.3390/min12121494

Zheng, H., Feng, X., and Hao, X. (2015). A creep model for weakly consolidated porous sandstone including volumetric creep. *Int. J. Rock Mech. Min.* 78 (0), 99–107. doi:10.1016/j.ijrmms.2015.04.021

Zheng, L., Wang, X., Lan, H., Ren, W., Tian, Y., Xu, J., et al. (2024). Study of the development patterns of water-conducting fracture zones under karst aquifers and the mechanism of water inrush. *Sci. Rep-Uk* 14 (1), 20790. doi:10.1038/s41598-024-71853-x

Zhu, L., Song, T., Gu, W., Xu, K., Liu, Z., Qiu, F., et al. (2022a). Study on layered-backfill-based water protection technology of thick coal seam in the ecologically fragile mining area in western China. *Geofluids* 2022, 1–16. doi:10.1155/2022/3505176

Zhu, Z., Zhu, Z., Wu, Y., and Liang, Z. (2022b). Mining-induced stress and ground pressure behavior characteristics in mining a thick coal seam with hard roofs. *Front. Earth Sc-Switz* 10, 843191. doi:10.3389/feart.2022.843191